Mercury's surface magnetic field determined from proton-reflection magnetometry

Reka M. Winslow[1], Catherine L. Johnson[1,2], Brian J. Anderson[3], Daniel J. Gershman[4,5], Jim M. Raines[4], Robert J. Lillis[6], Haje Korth[3], James A. Slavin[4], Sean C. Solomon[7,8], Thomas H. Zurbuchen[4], and Maria T. Zuber[9]

[1]Department of Earth, Ocean and Atmospheric Sciences, University of British Columbia, Vancouver, British Columbia, Canada, [2]Planetary Science Institute, Tucson, Arizona, USA, [3]The Johns Hopkins University Applied Physics Laboratory, Laurel, Maryland, USA, [4]Department of Atmospheric, Oceanic and Space Sciences, University of Michigan, Ann Arbor, Michigan, USA, [5]Geospace Physics Laboratory, NASA Goddard Space Flight Center, Greenbelt, Maryland, USA, [6]Space Sciences Laboratory, University of California, Berkeley, California, USA, [7]Lamont-Doherty Earth Observatory, Columbia University, Palisades, New York, USA, [8]Department of Terrestrial Magnetism, Carnegie Institution of Washington, Washington, District of Columbia, USA, [9]Department of Earth, Atmospheric and Planetary Sciences, Massachusetts Institute of Technology, Cambridge, Massachusetts, USA

Abstract Solar wind protons observed by the MESSENGER spacecraft in orbit about Mercury exhibit signatures of precipitation loss to Mercury's surface. We apply proton-reflection magnetometry to sense Mercury's surface magnetic field intensity in the planet's northern and southern hemispheres. The results are consistent with a dipole field offset to the north and show that the technique may be used to resolve regional-scale fields at the surface. The proton loss cones indicate persistent ion precipitation to the surface in the northern magnetospheric cusp region and in the southern hemisphere at low nightside latitudes. The latter observation implies that most of the surface in Mercury's southern hemisphere is continuously bombarded by plasma, in contrast with the premise that the global magnetic field largely protects the planetary surface from the solar wind.

1. Introduction

A remarkable feature of Mercury's weak, internal magnetic field, indicated by orbital observations, is a ~480 km northward offset of the magnetic equator from the geographic equator [*Anderson et al.*, 2011, 2012; *Johnson et al.*, 2012]. The low magnetic field strength and the northward offset provide constraints on Mercury's enigmatic dynamo mechanism [*Stanley and Glatzmaier*, 2010] and lead to direct interactions between the solar wind and the planet's surface. The weak magnetic field allows precipitation of solar wind plasma to the surface in the region of the northern magnetospheric cusp. Because the surface magnetic field strength at any southern latitude is predicted to be weaker than that at the corresponding northern latitude, enhanced ion sputtering and space weathering in the southern hemisphere are possible but to date have been expected to occur mainly on the dayside, at high latitudes in the southern cusp region. In this study we apply proton-reflection magnetometry, adapted from electron reflectometry [*Lin et al.*, 1976; *Mitchell et al.*, 2001; *Lillis et al.*, 2008], to determine Mercury's surface magnetic field strength in both hemispheres and measure particle precipitation to the surface.

Electron reflectometry (ER) has been used at the Moon [*Lin et al.*, 1998], Mars [*Lillis et al.*, 2008], and Ganymede [*Williams et al.*, 1997] to sense remotely the magnetic field strength at the surface. ER depends on the magnetic mirroring effect, that is, the reflection of electrons by the gradient in the magnetic field strength along convergent field lines. Electrons that would mirror below the surface are lost, and the flux of reflected electrons exhibits a sharp drop at the pitch angle α (the angle between the particle velocity and the local magnetic field direction) that corresponds to mirroring at the surface. The in situ magnetic field together with the pitch angle of the last reflected electrons, the cutoff pitch angle, indicates the surface magnetic field strength. This technique has not yet been applied using protons.

At Mercury, protons with energies of 0.3–10 keV are regularly detected inside the magnetosphere [*Zurbuchen et al.*, 2011] by the Fast Imaging Plasma Spectrometer (FIPS) [*Andrews et al.*, 2007] on the MErcury Surface, Space ENvironment, GEochemistry, and Ranging (MESSENGER) spacecraft. The Energetic Particle Spectrometer [*Andrews*
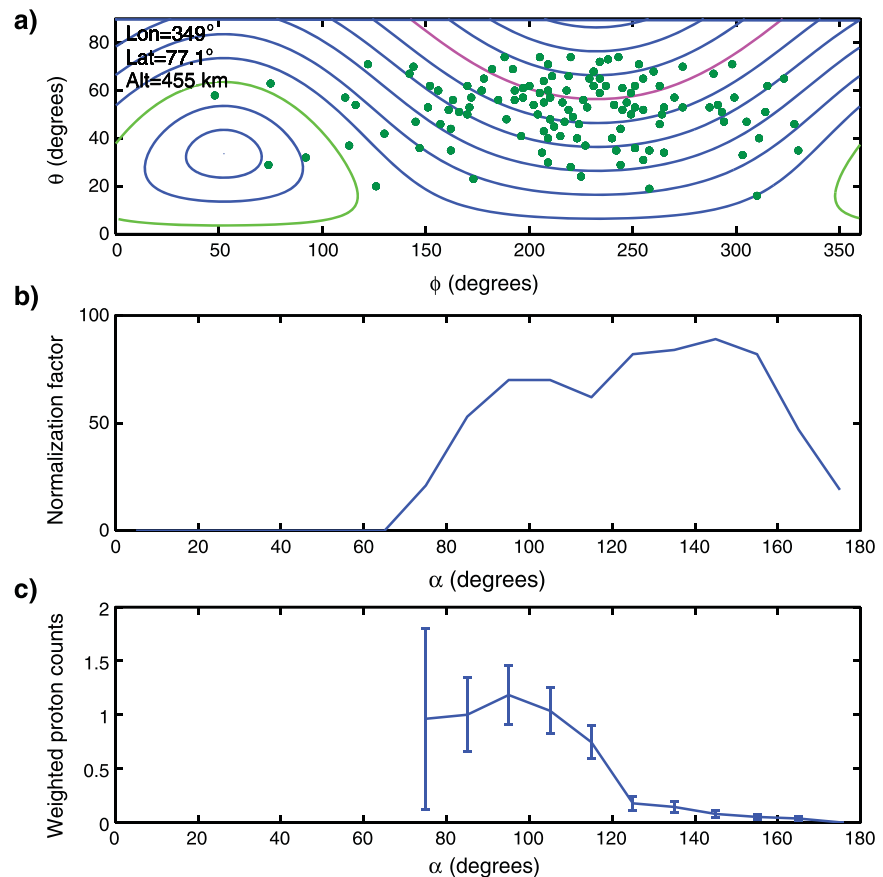
Figure 1. (a) Proton counts (green dots) versus zenith angle, θ, and azimuth angle, ϕ, in the FIPS reference frame, together with pitch angle contours for an example integration period (magenta contour is for $\alpha = 90°$, green contour is for $\alpha = 150°$, and the contour interval is 10°). The spacecraft longitude, latitude, and altitude are also given. (b) Time-normalization weighting factor as a function of α. (c) Derived PAD at this integration period.

et al., 2007] on MESSENGER detects electrons with energies only above 35 keV and observes substantial fluxes too infrequently to use ER. We therefore use FIPS observations of protons within Mercury's magnetosphere [*Winslow et al.*, 2013], together with the magnetic field observations from MESSENGER's Magnetometer (MAG) [*Anderson et al.*, 2007], to estimate the magnetic field strength at Mercury's surface.

2. Deriving Pitch Angle Distributions

For our analyses, we used one Earth year of observations, from 7 June 2011 to 7 June 2012. Combining observations from MAG and FIPS allowed the calculation of proton pitch angle and the derivation of pitch angle distributions (PADs) within the magnetosphere.

FIPS measures energy per charge (E/q), time of flight, and arrival incidence angle for ions, and it completes one scan over the full range of E/q values every 8 s [*Raines et al.*, 2011]. The sensor has a conical field of view (FOV) of approximately 1.4π sr, with two symmetric cutouts of 15° aperture, one near the instrument's symmetry axis and another near the plane perpendicular to the symmetry axis. FIPS pulse height analysis (PHA) data specific to proton times of flight are used to create the proton PADs at each integration period of FIPS. The raw, three-dimensional PHA events (Figure 1a) were divided by the visible solid angle per detector pixel and the pixel-dependent microchannel plate (MCP) detector efficiency [*Raines et al.*, 2014]. Because only angular structure is of interest for these accumulations, proton events from all E/q steps were added together to improve the signal-to-noise ratio.

After rotating the vector magnetic field measured by MAG into the FIPS reference frame, pitch angles for all proton counts were computed. The solid-angle-weighted and MCP-normalized proton counts that fall
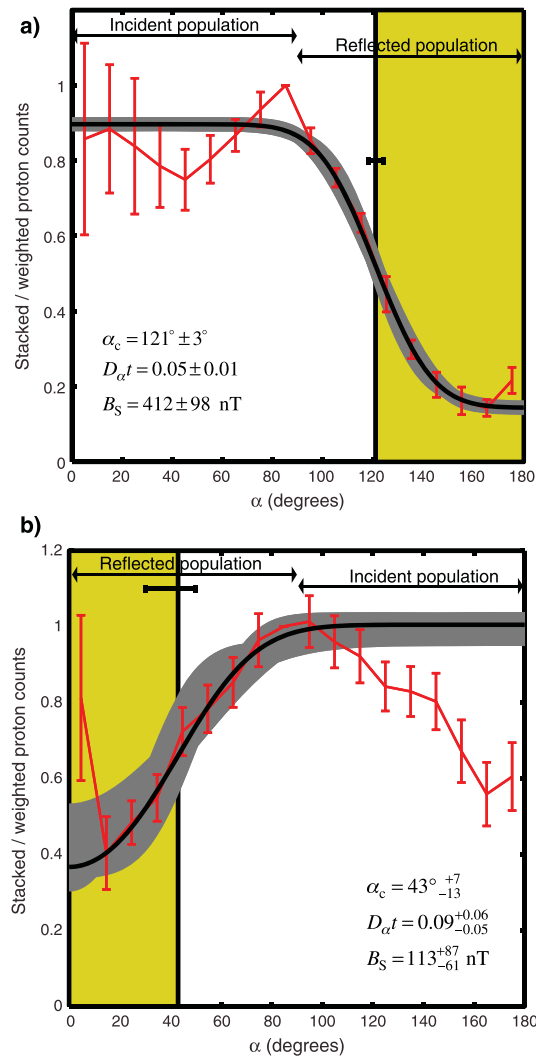
Figure 2. (a) PAD for Mercury's northern cusp. (b) PAD for the low-latitude southern hemisphere nightside. Average proton counts are in red with standard errors. The black curve shows the diffusion model fit to the reflected portion of the distribution; the fit uncertainty is in gray. The yellow shading indicates the loss cone; the black error bar shows the uncertainty in α_c.

within 10° pitch angle contours were then summed into 10°-wide pitch angle bins, centered on pitch angles from 5° to 175°.

The accumulated proton events were divided by a time-normalization factor that takes into account the FIPS visibility of each magnetic pitch angle bin [*Raines et al.*, 2014]. This normalization is a function of the FIPS orientation with respect to the magnetic field direction and FOV obstructions at each integration time (Figure 1b). We thus arrive at a PAD at every integration time, for which the proton counts have been properly weighted in order to take into account all the viewing limitations (Figure 1c). Errors assigned to each pitch angle bin center incorporate counting statistics and the fraction of proton gyrophase angles that was visible in the FOV for each pitch angle bin.

Because of the limited field of view of FIPS, the full proton PAD from $\alpha = 0°$ to 180° is not visible at any one integration time. To build PADs spanning $\alpha = 0°$ to 180° at times when the spacecraft was over the same location in Mercury solar orbital (MSO) coordinates (for which $+X$ is sunward, $+Z$ is northward, and $+Y$ completes the right-handed system), we combined and averaged PADs from times when the incident population was observed with PADs obtained when the reflected population was visible. We focused on regions where the highest proton counts were detected by FIPS. This analysis thus yields Mercury's average long-wavelength (e.g., dipole) surface magnetic field structure but does not resolve shorter-wavelength structure.

To connect the incident and reflected populations from different integration periods, we normalized each individual PAD by the weighted proton count observed at $\alpha = 85°$ or 95°, depending on which of the two pitch angles was visible in the distribution at that time, to approximate the average incident population. This methodology follows that applied to electron reflectometry measurements at the Moon [*Halekas et al.*, 2001]. We then computed the weighted averages of the individual PADs, where the inverse of the error at each pitch angle bin center on the PADs was assigned as the weight. The error assigned to the final averaged distribution is 1 standard error in all the proton counts averaged at each pitch angle bin center.

3. Surface Field Estimates

Averaged PADs were derived in the northern magnetospheric cusp region (geographic latitude $\lambda > 60°$N), as well as in regions of high proton flux on the nightside at low latitudes ($0° < \lambda < 30°$S) in the southern hemisphere. Although high proton fluxes to the dayside, in the southern cusp region, are expected, MESSENGER is unable to measure these, because its eccentric orbit allows the spacecraft to be inside the magnetosphere on the dayside only over northern latitudes. The averaged PAD for the northern cusp, which includes 485 reflected and 185 incident-population scans, is shown in Figure 2a. The incident population is approximately independent of pitch angle (i.e., isotropic), consistent with protons entering
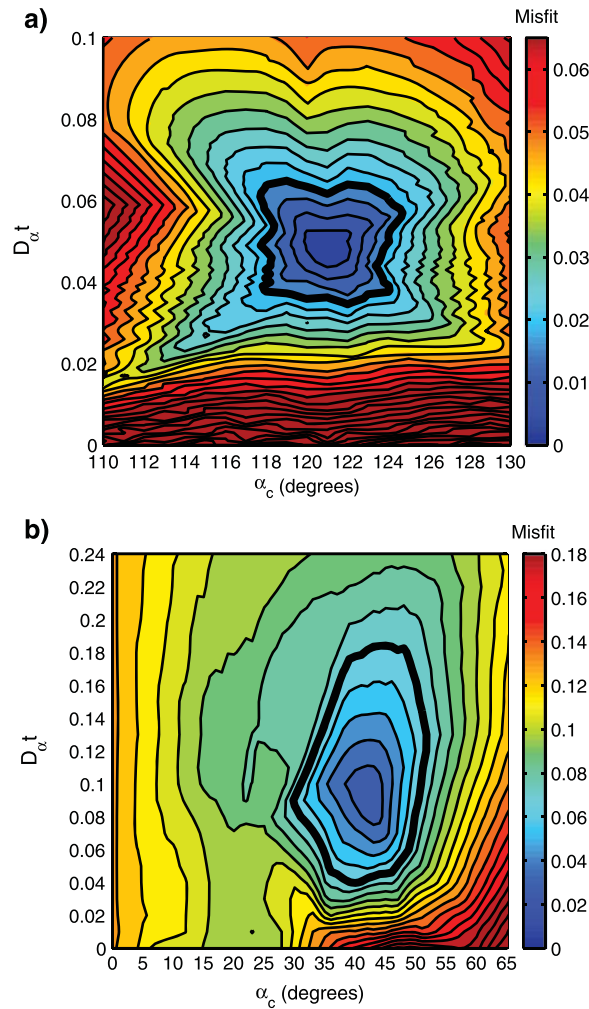
a)

b)

Figure 3. (a) Absolute values of misfit of the diffusion model to the PAD in the northern cusp, as a function of α_c and $D_\alpha t$. The bold contour marks the upper bound on the misfit level from which the errors on the fit parameters were obtained. (b) Same as in Figure 3a but for the southern hemisphere PAD. The ratio of the bold contour misfit level to the minimum misfit is ~7 in Figure 3a and ~3 in Figure 3b.

along open field lines from the magnetosheath. However, there is a loss cone in the fluxes of reflected protons, from $\alpha \sim 120°$ to 180°, evidence for incident protons having been "lost" to Mercury's surface. Relative to the sharp cutoff pitch angle observed in ER at the Moon [*Mitchell et al.*, 2008], the edge of the proton loss cone is smoothed over ~30° in α. We attribute this more gradual transition to the combined effects of the FIPS angular resolution of ~15° and pitch angle diffusion from wave-particle scattering in the cusp. Broadband magnetic field fluctuations of 0.001–10 Hz frequency are consistently observed in this region [*Anderson et al.*, 2013] and would pitch angle scatter protons.

We estimated the loss cone angle consistent with diffusive scattering by fitting solutions to the diffusion equation to the loss cones of our pitch angle distributions. We solved the one-dimensional diffusion equation

$$\frac{\partial u(\alpha, t)}{\partial t} = D_\alpha \frac{\partial^2 u(\alpha, t)}{\partial \alpha^2}, \tag{1}$$

where u is the proton count, t is the time over which diffusion occurs in the PAD, and D_α is the diffusion coefficient, with a step function initial condition:

$$u(\alpha, 0) = \begin{cases} c_1, & \alpha \leq \alpha_c \\ c_2, & \alpha > \alpha_c \end{cases}, \tag{2}$$

where c_1 and c_2 are constants set by the average maximum and minimum weighted proton counts in the PAD. The boundary conditions were given by

$$\frac{\partial u(0, t)}{\partial \alpha} = \frac{\partial u(\pi, t)}{\partial \alpha} = 0. \tag{3}$$

The solution to equation (1) is

$$u(\alpha, t) = \sum_{n=1}^{\infty} B_n \cos(n\alpha) e^{-n^2 D_\alpha t}, \tag{4}$$

where

$$B_n = \frac{2}{\pi} \left[\int_0^{\alpha_c} c_1 \cos(n\alpha) d\alpha + \int_{\alpha_c}^{\pi} c_2 \cos(n\alpha) d\alpha \right]. \tag{5}$$

We fit equations (4) and (5) to our loss cones allowing the cutoff pitch angle, α_c, and $D_\alpha t$ to vary. We used a grid search method that minimized the median absolute deviation between the model and the observations.
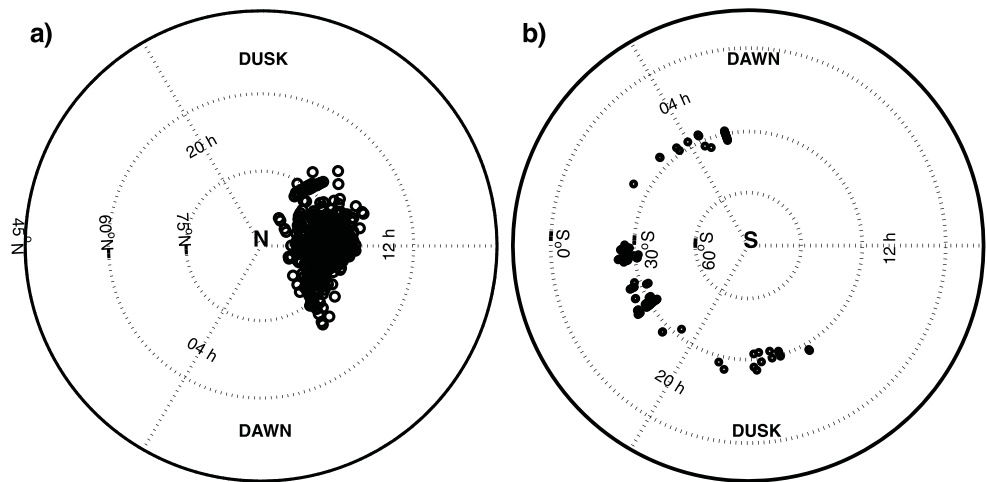
Figure 4. (a) Stereographic projection (looking at the planet from above the north pole) of surface magnetic foot-point locations of reflected proton observations in the northern cusp. The Sun is to the right. (b) Corresponding plot for the southern hemisphere (looking at the planet from above the south pole).

Figure 3 shows the contour plots of the absolute value of this misfit measure for the models best fit to the averaged PADs. We established the upper and lower bounds on the parameters α_c and $D_\alpha t$ by identifying an allowable upper bound on the misfit, corresponding to a 95% confidence limit (bold contours in Figure 3). The upper and lower bounds on α_c were identified as the locations of the intersection of a horizontal cut (passing through the minimum misfit) with the bold contour. A corresponding vertical cut yielded the limits on the $D_\alpha t$ parameter. The bounds on the best fit model, shown by the gray shaded regions of Figure 2, were determined from the diffusion curves corresponding to the upper and lower limits for α_c and $D_\alpha t$.

From the fit to the northern cusp PAD, we obtain a cutoff pitch angle of 121°±3°, which together with the measured average magnetic field strength at spacecraft altitudes (<550 km), $B_0 = 302.4 \pm 53.0$ nT, implies a surface field strength of $B_s = 412 \pm 98$ nT from the relation $B_s = B_0/\sin^2(\alpha_c)$. The uncertainty accounts for the standard error in the fit value of α_c and also the standard deviation of B_0, computed from all the intervals in the average PAD.

We mapped the observation locations in the cusp to the surface by tracing field lines to the surface given Mercury's offset dipole field. The observation altitudes ranged from 282 km to 549 km, with a mean of 414 km. Cusp observations traced to the surface extended 15.6° in latitude and 7.5 h in local time and were centered on noon at 76.4°N latitude (Figure 4a).

We also find high proton fluxes in the latitudinal band $0° < \lambda < 30°$S on the nightside, with a clear loss cone signature in the PAD (Figure 2b), although with larger uncertainties than for the northern cusp (Figure 2a). In the southern hemisphere, observations as far south as possible are desirable for observing the long-wavelength structure of the magnetic field. However, because of MESSENGER's eccentric orbit, we are restricted to observations north of ~30°S latitude. In this averaged PAD, we included 128 scans in the reflected population and 315 scans in the incident population. The similar errors on most of the proton fluxes in Figure 2b, despite the higher number of observations included for the incident side, result from large standard deviations in the incoming fluxes. The diffusion model that best fits the loss cone gives $\alpha_c = 43°^{+7}_{-13}$, and this value together with $B_0 = 52.5 \pm 14.8$ nT at the spacecraft altitude corresponds to a surface field of $B_s = 113^{+87}_{-61}$ nT. The observation altitudes were higher than those in the northern cusp, ranging between 1160 and 1980 km, with a mean of 1535 km. The mapped surface locations span $23°$S $< \lambda < 34°$S, with a mean of 27.8°S, and local times spanning the nightside from 16 h to 5.3 h, centered on 23.5 h (Figure 4b). The apparent secondary loss cone in the incident population in Figure 2b implies that these observations correspond to closed field lines on the nightside.

4. Discussion and Conclusions

The estimates of surface magnetic field strength are compared with predictions from the best fit time-averaged magnetospheric model of *Johnson et al.* [2012] in Figure 5 and Table 1. The results from proton-
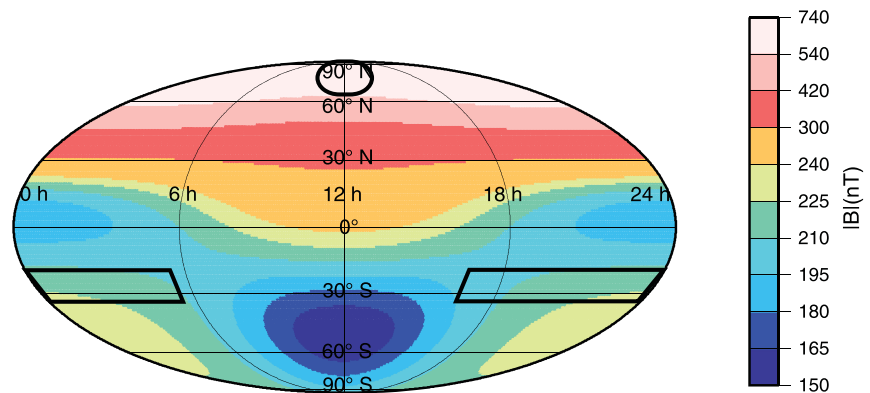
Figure 5. Surface magnetic field strength from the best fit magnetospheric model in MSO coordinates, Mollweide projection. The offset of the magnetic equator from the geographic equator and the magnetopause and magnetotail fields cause departures from the field of a centered dipole alone. The heavy black lines mark the approximate outline of regions sampled by proton-reflection magnetometry.

reflection magnetometry are markedly lower than the model magnetic field. Such a difference is expected, however, because the model is for a vacuum magnetic field, whereas our PADs demonstrate the presence of plasma that extends to the surface. The plasma generates a diamagnetic field, which reduces the surface field below the vacuum model prediction [*Korth et al.*, 2011, 2012; *Winslow et al.*, 2012].

Fortunately, the proton data provide the information required to estimate the diamagnetic effect. The particle flux at the surface in the northern cusp can be determined from the loss cone size and mean proton temperature, T_p, and density, n_p, in the cusp, yielding the proton pressure $P_p = n_p k T_p$, where k is Boltzmann's constant. The typical proton density ($n_p \approx 30\,\text{cm}^{-3}$) and temperature ($T_p \approx 12\,\text{MK}$) derived from FIPS observations in the cusp [*Raines et al.*, 2014] are for an isotropic particle distribution; the anisotropy associated with the loss cone produces an underestimate of plasma density [*Gershman et al.*, 2013]. Taking this anisotropy into account yields a surface flux of 3.7×10^{12} particles $\text{m}^{-2}\,\text{s}^{-1}$, which is approximately in agreement with the flux determined by *Winslow et al.*, [2012] for the cusp region. For our southern hemisphere average, we have $n_p \approx 5\,\text{cm}^{-3}$ and $T_p \approx 20\,\text{MK}$, which give a flux of 4.4×10^{11} particles $\text{m}^{-2}\,\text{s}^{-1}$. The diamagnetic effect reflects particle motions only in the direction perpendicular to the magnetic field, so we used the perpendicular particle pressure to calculate the diamagnetic field at the surface. We find an average diamagnetic effect, ΔB_{Plasma}, in the northern cusp of $86 \pm 11\,\text{nT}$ and $\Delta B_{\text{Plasma}} = 44 \pm 6\,\text{nT}$ in the southern hemisphere region. Uncertainties in these values represent the limits on the diamagnetic field derived from the pressure at the spacecraft altitude and that at the surface. After accounting for this effect, our magnetic field estimates agree with the model predictions in the southern hemisphere and are within 8% (our upper bound) of the model in the northern cusp (Table 1).

The validity of the offset dipole can be tested by estimating the ratio between the surface magnetic field strength in the northern cusp and that in the southern hemisphere. From the mean observation locations, we find that the ratio from proton-reflection magnetometry, corrected for the diamagnetic effect, is $3.2^{+3.0}_{-1.6}$, in agreement with the result of 3.3 for an offset dipole field alone. The full magnetospheric model [*Johnson et al.*, 2012] yields a surface field ratio of 2.6 to 3.6 for the latitudinal and longitudinal extent of our

Table 1. Surface Magnetic Field Strength From Proton-Reflection Magnetometry Compared With Magnetospheric Model Predictions

Latitude[a] (MSO Surface)	Local Time[a] (MSO)	B_{PR} (nT)[b]	B_{Plasma} (nT)	$B_{\text{PR}} - B_{\text{Plasma}}$ (nT)	B_{Model} (nT)[c]
76.4°N	12 h	412 ± 98	-86 ± 11	498 ± 99	647
27.8°S	23.5 h	113^{+87}_{-61}	-44 ± 6	157^{+87}_{-61}	224

[a]Central latitudes and local times of the two PADs.
[b]Surface magnetic field estimates from proton-reflection magnetometry.
[c]Magnetospheric model predictions for comparison with estimates from proton reflectometry corrected for plasma effects.

observation locations, with a mean value of 2.9. A centered dipole field alone gives a ratio of 1.5 for the latitudes sampled and is not in agreement with our inferred surface field ratio.

Proton-reflection magnetometry thus provides independent confirmation of the offset dipole nature of Mercury's magnetic field, although weaker terms of higher degree and order in a multipole expansion of the field are not ruled out by these results. Significantly, proton-reflection magnetometry demonstrates that persistent proton precipitation to the surface occurs on the nightside of Mercury's low-latitude southern hemisphere. This result implies that such precipitation may also be occurring at mid-southern latitudes on the nightside, where closed field lines reach the surface, because the northward offset of the magnetic equator results in weak surface field strengths (not more than 25% above the value from proton-reflection magnetometry) everywhere in the southern hemisphere. Together with the proximity of the magnetopause to the surface and the large cusp region on the dayside southern hemisphere [*Anderson et al.*, 2011, 2012; *Winslow et al.*, 2012], this finding suggests that most of Mercury's southern hemisphere surface may be continuously bombarded by plasma. Such precipitation in the southern hemisphere implies that space weathering is not confined to the cusp and may thus show limited latitudinal variation. Because of MESSENGER's eccentric orbit, proton-reflection magnetometry on the nightside at higher southern latitudes is not feasible, but observations from the ESA-JAXA BepiColombo mission [*Benkhoff et al.*, 2010], with a less eccentric orbit that will provide low-altitude observations in both hemispheres, may provide an opportunity to probe the surface field more extensively.

References

Anderson, B. J., M. H. Acuña, D. A. Lohr, J. Scheifele, A. Raval, H. Korth, and J. A. Slavin (2007), The Magnetometer instrument on MESSENGER, *Space Sci. Rev.*, *131*, 417–450, doi:10.1007/s11214-007-9246-7.

Anderson, B. J., C. L. Johnson, H. Korth, M. E. Purucker, R. M. Winslow, J. A. Slavin, S. C. Solomon, R. L. McNutt Jr., J. M. Raines, and T. H. Zurbuchen (2011), The global magnetic field of Mercury from MESSENGER orbital observations, *Science*, *333*, 1859–1862, doi:10.1126/science.1211001.

Anderson, B. J., C. L. Johnson, H. Korth, R. M. Winslow, J. E. Borovsky, M. E. Purucker, J. A. Slavin, S. C. Solomon, M. T. Zuber, and R. L. McNutt Jr. (2012), Low-degree structure in Mercury's planetary magnetic field, *J. Geophys. Res.*, *117*, E00L12, doi:10.1029/2012JE004159.

Anderson, B. J., C. L. Johnson, and H. Korth (2013), A magnetic disturbance index for Mercury's magnetic field derived from MESSENGER Magnetometer data, *Geochem. Geophys. Geosyst.*, *14*, 3875–3886, doi:10.1002/ggge.20242.

Andrews, B. G., et al. (2007), The Energetic Particle and Plasma Spectrometer instrument on the MESSENGER spacecraft, *Space Sci. Rev.*, *131*, 523–556, doi:10.1007/s11214-007-9272-5.

Benkhoff, J., J. van Casteren, H. Hayakawa, M. Fujimoto, H. Laakso, M. Novara, P. Ferri, H. R. Middleton, and R. Ziethe (2010), BepiColombo – Comprehensive exploration of Mercury: Mission overview and science goals, *Planet. Space Sci.*, *58*, 2–20, doi:10.1016/j.pss.2009.09.020.

Gershman, D. J., J. A. Slavin, J. M. Raines, T. H. Zurbuchen, B. J. Anderson, H. Korth, D. N. Baker, and S. C. Solomon (2013), Magnetic flux pileup and plasma depletion in Mercury's subsolar magnetosheath, *J. Geophys. Res. Space Physics*, *118*, 7181–7199, doi:10.1002/2013JA019244.

Halekas, J. S., D. L. Mitchell, R. P. Lin, S. Frey, L. L. Hood, M. H. Acuña, and A. B. Binder (2001), Mapping of crustal magnetic anomalies on the lunar near side by the Lunar Prospector electron reflectometer, *J. Geophys. Res.*, *106*, 27,841–27,852, doi:10.1029/2000JE001380.

Johnson, C. L., et al. (2012), MESSENGER observations of Mercury's magnetic field structure, *J. Geophys. Res.*, *117*, E00L14, doi:10.1029/2012JE004217.

Korth, H., B. J. Anderson, J. M. Raines, J. A. Slavin, T. H. Zurbuchen, C. L. Johnson, M. E. Purucker, R. M. Winslow, S. C. Solomon, and R. L. McNutt Jr. (2011), Plasma pressure in Mercury's equatorial magnetosphere derived from MESSENGER Magnetometer observations, *Geophys. Res. Lett.*, *38*, L22201, doi:10.1029/2011GL049451.

Korth, H., B. J. Anderson, C. L. Johnson, R. M. Winslow, J. A. Slavin, M. E. Purucker, S. C. Solomon, and R. L. McNutt Jr. (2012), Characteristics of the plasma distribution in Mercury's equatorial magnetosphere derived from MESSENGER Magnetometer observations, *J. Geophys. Res.*, *117*, A00M07, doi:10.1029/2012JA018052.

Lillis, R. J., D. L. Mitchell, R. P. Lin, and M. H. Acuña (2008), Electron reflectometry in the martian atmosphere, *Icarus*, *194*, 544–561, doi:10.1016/j.icarus.2007.09.030.

Lin, R. P., K. A. Anderson, R. Bush, R. E. McGuire, and J. E. McCoy (1976), Lunar surface magnetic fields detected by the electron reflection method, *Proc. Lunar Sci. Conf. 7th*, 2691–2603.

Lin, R. P., D. L. Mitchell, D. W. Curtis, K. A. Anderson, C. W. Carlson, J. McFadden, M. H. Acuña, L. L. Hood, and A. Binder (1998), Lunar surface magnetic fields and their interaction with the solar wind: Results from Lunar Prospector, *Science*, *281*, 1480–1484, doi:10.1126/science.281.5382.1480.

Mitchell, D. L., R. P. Lin, C. Mazelle, H. Rème, P. A. Cloutier, J. E. P. Connerney, M. H. Acuña, and N. F. Ness (2001), Probing Mars' crustal magnetic field and ionosphere with the MGS Electron Reflectometer, *J. Geophys. Res.*, *106*, 23,419–23,427, doi:10.1029/2000JE001435.

Mitchell, D. L., J. S. Halekas, R. P. Lin, S. Frey, L. L. Hood, M. H. Acuña, and A. Binder (2008), Global mapping of lunar crustal magnetic fields by Lunar Prospector, *Icarus*, *194*, 401–409, doi:10.1016/j.icarus.2007.10.027.

Raines, J. M., J. A. Slavin, T. H. Zurbuchen, G. Gloeckler, B. J. Anderson, D. N. Baker, H. Korth, S. M. Krimigis, and R. L. McNutt Jr. (2011), MESSENGER observations of the plasma environment near Mercury, *Planet. Space Sci.*, *59*, 2004–2015, doi:10.1016/j.pss.2011.02.004.

Raines, J. M., D. J. Gershman, J. A. Slavin, T. H. Zurbuchen, H. Korth, B. J. Anderson, and S. C. Solomon (2014), Structure and dynamics of Mercury's magnetospheric cusp: MESSENGER measurements of protons and planetary ions, *J. Geophys. Res. Space Physics*, in press, doi:10.1002/2014JA020120.

Stanley, S., and G. A. Glatzmaier (2010), Dynamo models for planets other than Earth, *Space Sci. Rev.*, *152*, 617–649, doi:10.1007/s11214-009-9573-y.

Williams, D. J., et al. (1997), Energetic particle signatures at Ganymede: Implications for Ganymede's magnetic field, *Geophys. Res. Lett.*, *24*, 2163–2166, doi:10.1029/97GL01931.

Winslow, R. M., C. L. Johnson, B. J. Anderson, H. Korth, J. A. Slavin, M. E. Purucker, and S. C. Solomon (2012), Observations of Mercury's northern cusp region with MESSENGER's Magnetometer, *Geophys. Res. Lett.*, *39*, L08112, doi:10.1029/2012GL051472.

Winslow, R. M., B. J. Anderson, C. L. Johnson, J. A. Slavin, H. Korth, M. E. Purucker, D. N. Baker, and S. C. Solomon (2013), Mercury's magnetopause and bow shock from MESSENGER Magnetometer observations, *J. Geophys. Res. Space Physics*, *118*, 2213–2227, doi:10.1002/jgra.50237.

Zurbuchen, T. H., et al. (2011), MESSENGER observations of the spatial distribution of planetary ions near Mercury, *Science*, *333*, 1862–1865, doi:10.1126/science.1211302.